

Robust Mottness and tunable interlayer magnetism in Nb_3X_8 ($\text{X} = \text{F}, \text{Cl}, \text{Br}, \text{I}$) bilayers

Zhongqin Zhang^{1,2}, Jiaqi Dai^{1,2}, Cong Wang^{1,2}, Zhihai Cheng^{1,2}, and Wei Ji^{1,2*}

¹*Beijing Key Laboratory of Optoelectronic Functional Materials & Micro-Nano Devices, School of Physics, Renmin University of China, Beijing 100872, China*

²*Key Laboratory of Quantum State Construction and Manipulation (Ministry of Education), Renmin University of China, Beijing 100872, China*

* W.J. (email: wji@ruc.edu.cn)

Abstract:

Kagome materials have attracted extensive attention due to their correlated properties. The breathing kagome material system Nb_3X_8 ($\text{X} = \text{F}, \text{Cl}, \text{Br}, \text{I}$) is regarded as a Mott insulator. However, studies on the influence of interlayer coupling on its magnetic and Mott properties are lacking. In this work, we investigated the effect of interlayer coupling on bilayer properties of each Nb_3X_8 ($\text{X} = \text{F}, \text{Cl}, \text{Br}, \text{I}$) compound via density functional theory (DFT) calculations, considering 24 stacking configurations per material. We found that each bilayer material is a Mott insulator. Due to the competition between interlayer Pauli repulsion and hopping, most interlayer magnetism is AFM, a small number of cases show AFM-FM degeneracy, and the magnetic ground state of 3 configurations is interlayer FM, i.e., tunable interlayer magnetism occurs. This robustness of Mott states coexisting with tunable interlayer magnetism provide novel and comprehensive analysis and insights for the research of breathing kagome Mott insulators.

Keywords: kagome lattice; Mott insulator; van der Waals magnets; Nb_3Cl_8 ; Nb_3F_8 ; Nb_3Br_8 ; Nb_3I_8 .

Kagome-lattice materials are exceptional material platforms for exploring the interplay among electronic band topology, strong electron correlation, and magnetism in quantum materials[1–7]. The standard kagome tight-binding model is in two-dimensional (2D) and exhibits a flat band across the entire Brillouin zone, Dirac cones at the K points, and van Hove singularities located at the M points. Theoretical studies predict that tuning electron filling within these kagome bands can stabilize diverse exotic phases, such as magnetism[8,9], superconductivity[10,11], charge-density wave states[12]. Experimental investigations, however, have primarily focused on three-dimensional (3D) bulk kagome materials, such as CsV_3Sb_5 [7,13,14] and Co_3SnS_2 [15–17], where superconductivity[13,14], pair-density wave[7], charge order[13], and spin-orbit polarons[15] have been reported. In bulk crystals, intrinsic kagome layers typical alternate with spacer layers, whose strong interlayer hybridization[18] often shifts or even eliminates the characteristic kagome bands near the Fermi level[18,19], obscuring the exploration of intrinsic kagome physics.

Significant effort has recently been devoted to constructing 2D kagome lattices with minimal interlayer coupling [4]. Strategies include surface-assembled organic kagome monolayers[20–22], MoTe_{2-x} monolayers mirror-twin-boundary loops [23–25], atomic intercalation within van der Waals (vdW) layers[26,27], and a recently highlighted 3+1 protocol [28]. Among them, Nb_3X_8 ($\text{X} = \text{Cl}, \text{Br}, \text{I}$) is a prototypical layered breathing kagome family, with adjacent layers weakly coupled through vdW interactions[29–35]. Monolayers Nb_3Cl_8 and Nb_3Br_8 are established Mott insulators, characterized by well-defined upper and lower Mott-Hubbard bands around the Fermi level[31,36]. Their bulk counterparts, however, exhibit more complicated behaviors, particularly in magnetism[34,35]. Bulk Nb_3Cl_8 and Nb_3Br_8 undergo structural transitions at approximately 100 K and 380 K, respectively, accompanying by a magnetic transition from Curie-Weiss paramagnetism (PM) in the high-temperature (HT) phase to a likely nonmagnetic (NM) state at lower temperatures (LT) [34,35]. Interestingly, these contrasting magnetic states differ structurally in their stacking sequences only. Moreover, the two previously proposed mechanisms for the LT NM

state are both closely related to interlayer couplings[34,35], further highlighting the importance of interlayer interactions in Nb₃X₈.

Interlayer coupling, a unique feature of 2D materials, has increasingly recognized as an effective route to tune electronic band gaps[37,38], optical[39,40] and acoustic properties[41], magnetism[42–45], and electric polarization[46,47]. Recently, it was found that interlayer coupling in bilayer 1T-NbSe₂ can transform it from a correlated insulator into a nonmagnetic band insulator, raising a crucial question: what is the role of interlayer coupling on electronic structures of kagome-based Nb₃X₈ bilayers? In this letter, we theoretically investigated the roles of interlayer coupling in tuning the electronic structures and magnetism in Nb₃X₈ (X = F, Cl, Br, I) bilayers using density functional theory (DFT) calculations. We first identified out-of-plane (OOP) electric polarization and a robust Mott-Hubbard gap in Nb₃X₈ monolayers using spin polarized bandstructure calculations with varying U . Next, we compared the total energies of 24 stacking configurations for each compound among NM and interlayer AFM and FM states. Most bilayers favor interlayer AFM, while a few exhibit AFM-FM degeneracy. All bilayers remain Mott insulators, as verified by real-space wavefunction distributions, bandstructures, and U dependence. Symmetry analyses uncover compensated AFM states in parallel electric polarized stackings, classifying all studied configurations into three stacking-dependent and tunable interlayer magnetism. This robustness of Mott states coexisting with tunable interlayer magnetism contrasts sharply with the behaviors of transition-metal dichalcogenide-based Mott insulators.

Our density functional theory (DFT) calculations were performed using the generalized gradient approximation (GGA) for the exchange correlation potential in the form of Perdew-Burke-Ernzerhof (PBE)[48], the projector augmented wave method[49], and a plane-wave basis set as implemented in the Vienna ab-initio simulation package (VASP)[50]. The dispersion correction was included using Grimme's semiempirical D3 scheme[51] in combination with the PBE functional (PBE-D3). A kinetic energy cutoff of 450 eV for the planewave basis sets was adopted

for all structural relaxations and electronic structure calculations. All atoms were allowed to relax until the residual force per atom is below 0.01 eV/Å. A vacuum layer exceeding 15 Å in thickness was used to reduce imaging interactions from neighboring supercells. Gamma-centered Monkhorst-Pack k -meshes of $5\times5\times1$ and $9\times9\times1$ were used to sample the Brillouin zone of 1×1 unit cells for structural relaxations and electronic structure calculations, respectively. In comparison the energies of magnetic configurations, a $2\times\sqrt{3}$ supercell and a 4×5 k -mesh were employed. A Gaussian smearing width of 0.01 eV was used to smooth the distribution function of electronic states in all calculations. A DFT+ U method implemented using the rotationally invariant approach[52] was used to apply a series of Hubbard U values specifically to Nb $3d$ orbitals. Comparison of energies of different magnetic configurations were made based on the structures optimized for interlayer AFM coupling. Energy comparison based on the structures relaxed using interlayer FM does not change the relative energetic stability.

A free-standing Nb₃X₈ monolayer adopts a breathing kagome geometry [Fig. 1(a) and 1(b)], in which compact Nb₃ trimers (shaded in orange) corner-sharing with expanded Nb triangles (shaded in gray), giving rise to alternating short (d_{Nb1}) and long (d_{Nb2}) Nb–Nb bonds. The halogen atoms bonded to these triangular units form two inequivalent sublayers. In the lower sublayer, three equal-height halogen atoms lie beneath the expanded Nb triangle, giving a shorter vertical distance to the Nb plane (d_{XS}) than that of the halogens in the upper sublayer (d_{XL}). The remaining halogen atom in the lower sublayer, residing beneath the compact trimer [X-s, purple, Fig. 1(a) to 1(c)], is displaced further away from the Nb plane by Δ_{S} relative to the other three halogens in the same sublayer. In the upper sublayer, the halogen sitting above the expanded triangle (X-l, pink) is shifted closer to the Nb plane by Δ_{L} compared with the other three upper-sublayer halogens. We denote the lower and upper sublayers as X-s and X-l, respectively.

For Nb₃F₈, the Nb-Nb bond length in the Nb₃ trimer (d_{Nb1}) contracts to 2.59 Å, well below the Nb-Nb bonds in bulk Nb (approximately 2.86 Å), whereas in the other

Nb halides, d_{Nb1} is comparable to or larger than the bulk value. This pronounced contraction of d_{Nb1} indicates strong trimer compression and thereby enhances the X-s displacement (Δ_s). Table 1 compiles the two ratios Δ_s/d_{XS} and Δ_L/d_{XL} for all four Nb halides. With the sole exception of Δ_s/d_{XS} in Nb_3F_8 (0.44), which is anomalously large, the other seven entries decrease monotonically as X is varied from I to F. These opposite out-of-plane (OOP) displacements (Δ_s and Δ_L) and inequivalent distances (d_{XS} and d_{XL}) lead to a net OOP electric polarization for each Nb halide, with Nb_3F_8 exhibiting the largest value of 1.26 pC/m (Table 1, Fig. 1(c)).

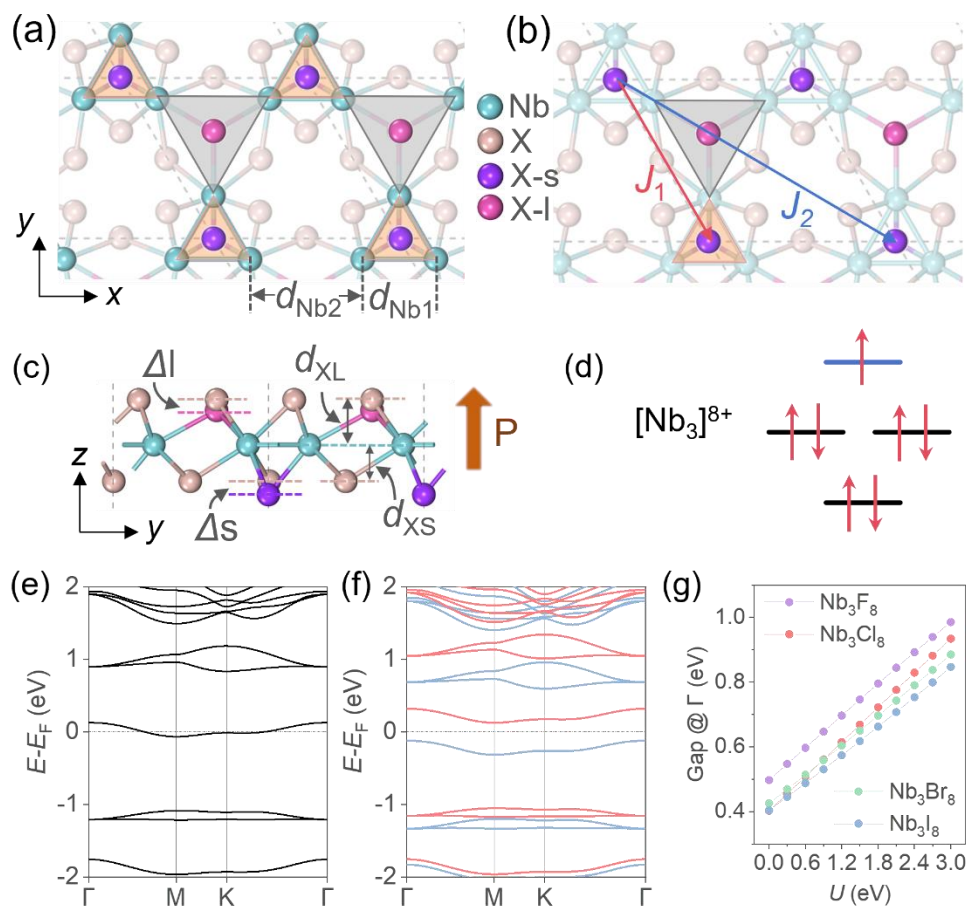


Fig. 1. (a-c) Top(a-b) and side(c) view of monolayer Nb_3X_8 . Nb atoms are represented by light sea green balls. The gray and orange shading indicate the large and small triangles formed by Nb atoms, with X atoms at the center of these triangles labeled as X-l and X-s, shown by pink and purple balls, and remaining X atoms are represented by light brown balls. The brown arrow and "P" denote the polarization direction. Red and blue arrows represent the nearest-neighbor and next-nearest-neighbor exchange couplings between Nb_3 trimers. Gray dash lines indicate the Nb-Nb distance within (d_{Nb1}) and between (d_{Nb2}) trimers. d_{XS} and d_{XL} represent the vertical displacements of corresponding X relative to Nb atomic layer, while Δ_s ,

Δ_L represent the vertical displacements of X-s and X-l atoms relative to the other three halogens in the same sublayer. (d) Electronic configuration of $[\text{Nb}_3]^{8+}$. (e-f) Band structures of Nb_3Cl_8 in NM (e) and FM (f) configurations. In (f), the blue and red bands represent the spin-up and spin-down channels. (g) Band gaps at the Γ point as a function of Hubbard U , calculated using the magnetic ground states.

We compared the total energies of seven magnetic configurations for each Nb_3X_8 monolayer for finding the most favored magnetic configuration among them, as shown in Supplementary Fig. S1. Triangularly arranged Nb atoms in a Nb_3 trimer have geometric frustration, which, however, favor a FM nearest neighboring coupling, thereby exhibiting a shared local magnetic moment on the trimer. Therefore, we treated the Nb_3 trimer as a single entity with the +8 oxidation state. The valence electron configuration of the trimer, as shown in Fig. 1d, includes one unpaired electron and six paired electrons, exhibiting a magnetic moment of $1 \mu_B$. Thus, the triangularly arranged trimers form a $S = 1/2$ triangular lattice site. While either the Nb_3Br_8 or Nb_3I_8 monolayer favors an FM configuration, Nb_3Cl_8 has nearly degenerate FM, ZZ-AFM and Stripe-AFM configurations, consistent with the literature [31,53,54]. However, the ZZ-AFM configuration is slightly stabilized in Nb_3F_8 (0.25 meV/ Nb_3 more stable than the stripe-AFM configuration). Based on energy comparisons among the various magnetic configurations, we calculated the nearest-neighbor (J_1) and next-nearest-neighbor (J_2) spin-exchange coupling constants among these Nb_3 trimers [indicated by red and blue arrows in Fig. 1(b)], which are summarized in Table 1. Each Nb_3X_8 monolayer exhibits easy-plane anisotropy, with the magnetic anisotropy energy ranging from 0.11 to 0.38 meV/ Nb_3 [Fig. S2, Table S2].

Monolayer Nb_3Cl_8 [31–33] or Nb_3Br_8 [29,30], has been identified as a Mott insulator in previous dynamical mean field theory (DMFT)[31,32] and model-based [29,30,33] calculations. A spin non-polarized DFT calculation for, for instance, Nb_3Cl_8 reveals a partial (half)-occupied spin-degenerate quasi-flat band that cuts the Fermi level, as plotted in Fig. 1(e). This degeneracy lifts in a spin polarization bandstructure with the FM configuration, splitting the partial occupied band into a fully occupied and an empty spin-polarized band [Fig. 1(f)], as a result of the electron exchange effect. To

capture strong electron correlations, incorporating an additional on-site Hubbard U energy corrects the self-interaction error of DFT and localizes electronic wavefunctions, and further enhances the exchange splitting. Consequently, the split gap at the Γ point grows linearly as a function of U [Fig. 1(g)], exhibiting a signature characteristic of Mott insulators. Our DFT+ U results thus confirm that all four Nb_3X_8 monolayers are Mott insulators, consistent with previous DMPT results [31–33,55,56].

Table 1 Lattice constants (a), Nb-Nb distance within (d_{Nb1}) and between (d_{Nb2}) Nb_3 trimers, vertical shift of X atoms (see Fig. 1(c)) , polarization (P , in units of pC/m), magnetic ground states (G. S.) and the nearest-neighbor (J_1) and next-nearest-neighbor (J_2) exchange couplings between Nb_3 trimers (in units of meV/ Nb_3) for monolayer Nb_3X_8 . Here, the magnetic coupling between Nb atoms within a Nb_3 trimer is FM. A positive value of the exchange constant indicates AFM coupling.

Halides	a	d_{Nb1}	d_{Nb2}	Δ_S	d_{XL}	Δ_S/d_{XL}	Δ_S	d_{XL}	Δ_S/d_{XL}	P	G. S.	J_1	J_2
	(Å)	(Å)	(Å)	(Å)	(Å)		(Å)	(Å)					
Nb_3F_8	5.95	2.59	3.36	0.48	1.10	0.44	0.23	1.35	0.17	1.26	ZZ	6.75	-0.49
Nb_3Cl_8	6.76	2.81	3.95	0.47	1.36	0.35	0.29	1.64	0.18	0.21	FM	0.12	-0.24
Nb_3Br_8	7.11	2.88	4.23	0.54	1.44	0.38	0.35	1.76	0.20	0.41	FM	-2.74	-0.37
Nb_3I_8	7.63	3.01	4.62	0.60	1.54	0.39	0.47	1.91	0.25	0.56	FM	-2.93	-0.82

We next investigate how interlayer couplings reshape the geometric and electronic structures of bilayer Nb_3X_8 . As the monolayer exhibits an intrinsic OOP polarization, the two layers can stack in three alignments, namely up-up (Fig. S9(h)), up-down [Fig. 2(a)], and down-up (Fig. S4(b-c)), which are label as UU, UD, and DU, respectively. Lateral stacking registries further differentiates the stackings. Figures 2(b) and 2(c) present the top-views of the up- and down-polarized bottom Nb_3X_8 layers, respectively, in which interfacial X and Nb atoms are highlighted and the outer X atoms are faded for clarity. We identify four inequivalent interfacial X triangles (shadowed in orange) with their hollow sites labelled 1 to 4, in either up- or down-polarization case. Taking the X-s atom of the top layer as a reference for alignment UD (for alignments UU and

DU, we take the X-l atom), sliding the top layer to align the X-s (or X-l) atom [Fig. 2(a)] occupying at any one of these sites constructs four distinct stacking configurations. A third degree of freedom is the relative twist between the two layers. We considered untwisted (R0) and 60° twisted (R60) bilayers, as shown in Fig. 2(d) and 2(e), respectively. Combining polarization (three alignments) with hollow site (four sites) and twist angle (two angles) yields 24 distinct stacking configurations per halide. We label them as (site)-(twist)-(polarization), for instance, 1-R0-UU corresponds to the AA stacking. Within this scheme, configurations 1-R60-DU, 4-R60-DU, and 2-R60-UD correspond to the experimentally observed H1 and L1 stackings in the high- (HT) and low-temperature (LT) phases, and their common stacking C2 of bulk Nb₃X₈, respectively (Fig. S3) [34,35,57–59].

Figures Fig. 2(f)-2(h) and S5 depict the total energies of all 24 Nb₃X₈ bilayer stackings in the NM, interlayer FM, and interlayer AFM configurations, while Fig. S6 presents the corresponding interlayer distance. The four halides exhibit halogen dependent trends in their relative energy profiles. For Nb₃Cl₈, Nb₃Br₈ and Nb₃I₈, the global energy minimum corresponds to the 2-R60-UD stacking (C2), whereas Nb₃F₈ favors the 3-R60-UD (AS) configuration over C2. The preference of C2 in Nb₃Cl₈ to Nb₃I₈ rationalizes the experimentally observed bilayer dimerization (with the C2 stacking) in its LT and HT bulk forms. By contrast, Nb₃F₈ is expected to adopt a different pairing registry. Because the C2 (or AS) stacking adopts a UD polarization alignment, the stacking registry between paired C2 bilayers in bulk Nb₃X₈ must be of the DU alignment. Among all DU configurations (yellow in Figs. 2f to 2h, and S5), the L1 stacking is consistently the most stable, while H1 is the second-lowest in energy only for Nb₃Cl₈. For DU stackings related to L1 by in-plane translation (i.e. without rotation), the most stable registry is 2-R60-DU for Nb₃F₈ and 3-R60-DU for Nb₃Br₈ and Nb₃I₈. These results suggest that bulk Nb₃F₈ in its LT phase adopts interleaved sequence of AS and L1 bilayers, a geometry distinct from the C2-based stacking sequences found in the heavier halides.

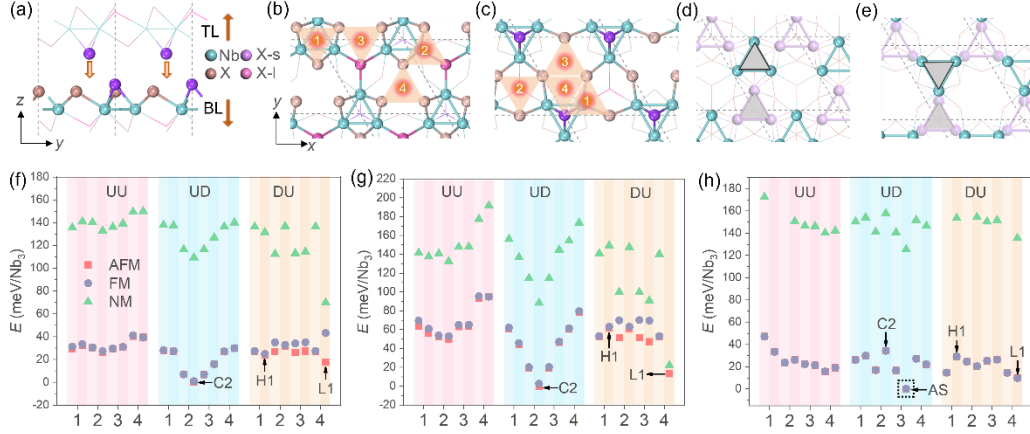


Fig. 2. (a) Side view of the fully relaxed atomic structure of a Nb₃X₈ bilayer. Interfacial X-s atoms of the top layer, and all interfacial X and Nb atoms of the bottom layer are highlighted, while other atoms are represented using lines. Brown arrows indicate the polarization directions of the top (TL) and bottom (BL) layers, respectively. (b-c) top-views of the atomic structure of the bottom layer in up- and down-polarizations, respectively. Shaded numbers 1 to 4 mark four inequivalent X-hollow positions at the interface. All X atoms in the surface sublayer are blurred using line models. (d-e) Schematics of untwisted (R0, d) and 60° twisted (R60, e) bilayers. All X atoms are blurred using lines to highlight the relative position of top (light sea green) and bottom (light purple) layer Nb atoms. Gray shaded triangles indicate Nb₃ trimers. (f-h) Energies of all 24 stacking configurations for bilayer Nb₃Cl₈ (f), Nb₃I₈ (g) and Nb₃F₈ (h) with a 1.2 eV U value (h). Square, circle, and triangle symbols represent interlayer AFM, FM, and NM, respectively. Notation ZZ represents the intralayer zigzag magnetic configuration. Red, blue, and yellow shaded blocks represent polarization directions of UU, UD and DU, respectively. The light and dark shaded blocks represent R0 and R60, respectively. The energy of the most stable stacking in each material is set as the reference (zero) energy.

In Nb₃F₈ bilayers, the most stable stacking is AS (3-R60-UD), rather than the C2 (2-R60-UD) configuration that dominates in Nb₃Cl₈, Nb₃Br₈, and Nb₃I₈. This contrast highlights the distinct structural preference of Nb₃F₈. In the UD configurations, the interfacial halogen atoms form four inequivalent triangles [highlighted by orange shadows in Fig. 2(c)], whose side lengths are listed in Table 2. In Nb₃Cl₈, Nb₃Br₈, and Nb₃I₈, triangle 2 exhibits the longest side length, resulting in the lowest electronic density. When the X-s atom in the top layer is positioned at the center of the triangle 2, the Coulomb repulsion between the X atoms within the triangles and the X-s atoms is

minimized. This, in turn, results in the lowest energy for the 2-R60-UD stacking and the smallest interlayer distance [Fig. S6]. In contrast, in Nb_3F_8 , the triangles undergo disproportionation, leading to the shortest side length for triangle 2 (2.82 Å) and the longest for triangle 3 (3.12 Å). Consistent with the relationship established earlier, the longest side length of triangle 3 gives rise to its lowest electron density, thereby resulting in the lowest energy and interlayer distance when the upper X-s atom is positioned on triangle 3. Consequently, in Nb_3F_8 , the 3-R60-UD (AS) configuration exhibits the lowest energy.

We next take bilayer Nb_3Cl_8 in the representative L1 (4-R60-du) stacking configuration as a prototype to elucidate the role of interlayer coupling in modulating electronic structure. In previous studies, the L1 stacking configuration was considered to possess a NM ground state[32,60]; accordingly, we first examine the NM case. Figure 3(a) plots a spin non-polarized bandstructure of bilayer Nb_3Cl_8 . Upon stacking two monolayers, the partially occupied flat bands originally present in isolated monolayers split into fully occupied valence band (VB1) and a completely empty conduction band (CB1). Both are spin-degenerate and located near the Fermi level. Wavefunction norm visualizations indicate that VB1 corresponds to a bonding state primarily localized on interfacial Cl atoms [Figs. 3(b)], while CB1 is antibonding between two interfacial Cl sublayers [Figs. 3(c)]. This interlayer orbital hybridization corresponds to the energy splitting of flat bands in the nonmagnetic bilayer.

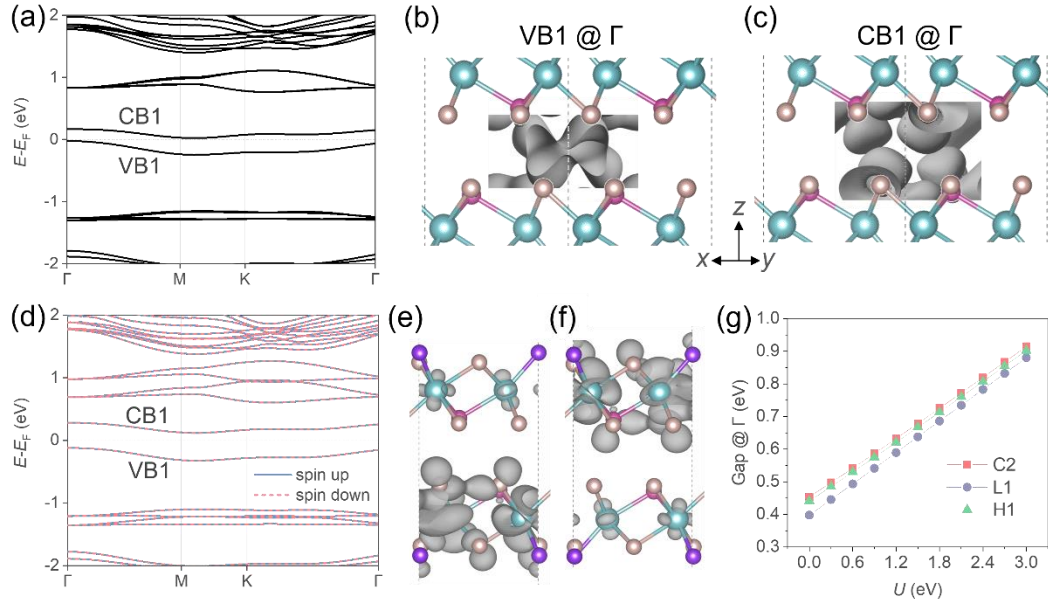


Fig. 3 (a) Electronic band structure of Nb_3Cl_8 with L1 stacking in the NM state. (b-c) Side views of Nb_3Cl_8 with L1 stacking. (d) Electronic band structure of Nb_3Cl_8 with L1 stacking in the interlayer AFM state. The isosurface represents the visualized wavefunction norms of the VB1 (b) and CB1 (c) at the Γ point. The isosurface value was set to $3 \times 10^{-4} \text{ e/Bohr}^3$. (e-f) Visualized wavefunction norms of the VB1 for spin-up (g) and spin-down (h) components. The isosurface value was set to $5 \times 10^{-4} \text{ e/Bohr}^3$. (g) Band gaps at the Γ point as a function of Hubbard U , calculated using interlayer AFM configurations.

In comparison to Fig. 3(a), we plotted the corresponding spin polarized bandstructure with the interlayer AFM coupling in Fig. 3(d). This AFM state is 19.4 meV/ Nb_3 more stable than its spin non-polarized NM state. Similar to the NM case, the electronic structure near the Fermi level comprises two sets of flat bands, namely a fully occupied VB1 and an empty CB1 band, separated by a bandgap of 0.40 eV at the Γ point. Each band set consists of two energetically degenerate but spatially distinct spin-polarized states. Visualized wavefunction norms at Γ clearly demonstrate a layer-dependent spin locking that the spin-up component of VB1 predominantly localizes on the bottom layer [Fig. 3(e)], whereas the spin-down component resides mainly on the top layer [Fig. 3(f)]. This layer-spin locking is a general feature for all bands near the Fermi level. Specifically, the spatial wavefunction distributions of spin-up and spin-

down states in CB1 [Figs. S8(a,b)] closely mirror those of spin-down and spin-up states in VB1, respectively. Consequently, each layer hosts energetically separated spin-polarized states with opposite spin alignments between layers, consistent with the characteristic of AFM-coupled Mott insulator. Furthermore, the bandgap at Γ exhibits a linear dependence on the applied Hubbard U value [Fig. 3(i)], clearly identifying it as a Mott–Hubbard gap, with VB1 and CB1 corresponding to the lower Hubbard band (LHB) and upper Hubbard band (UHB), respectively. Such a linear gap- U dependence is universal across all 24 stacking configurations of the four Nb_3X_8 bilayers studied, as illustrated by representative stacking orders C2, L1, and H1 of bilayer Nb_3Cl_8 in Fig. 3(g). These results highlight the robustness of these Mott insulator characteristics in Nb_3X_8 bilayers.

We use the Nb_3Cl_8 L1 and C2 stacking configurations as examples to investigate the impact of different polarization alignments on the electronic structure. Fig. 4(a-b) depict the structure and interlayer differential charge density (DCD) for the L1 stacking. At the interface, the two triangulars labeled as triangle 2 [Figs. 2(b), light brown atoms in the dashed box in Fig. 4(b)] from the top and bottom layers are aligned with a relative 60° twist. Within these triangles the electronic density is depleted, with the excess charge redistributed mainly to regions outside the triangles and partially into the interlayer region. The reduced charge density inside the triangles lowers the Coulomb repulsion among the three X atoms and hence shortens the triangle side length (from 3.42 Å in the monolayer to 3.34 Å in the L1 stacking). The interlayer charge accumulation enhances the electrostatic attraction between the two layers. In the C2 stacking configuration [Figs. 4(c-d)], the X-s atoms exhibit charge depletion, while the three nearest X atoms (assigned to triangle 2 in Fig. 2(c), light brown atoms in dashed boxes in Fig. 4(d)) in the opposing layer undergo charge accumulation. This charge redistribution gives rise to the formation of local dipoles oriented along the vertical direction. These oppositely aligned dipoles enhance the interlayer attraction via electrostatic interactions.

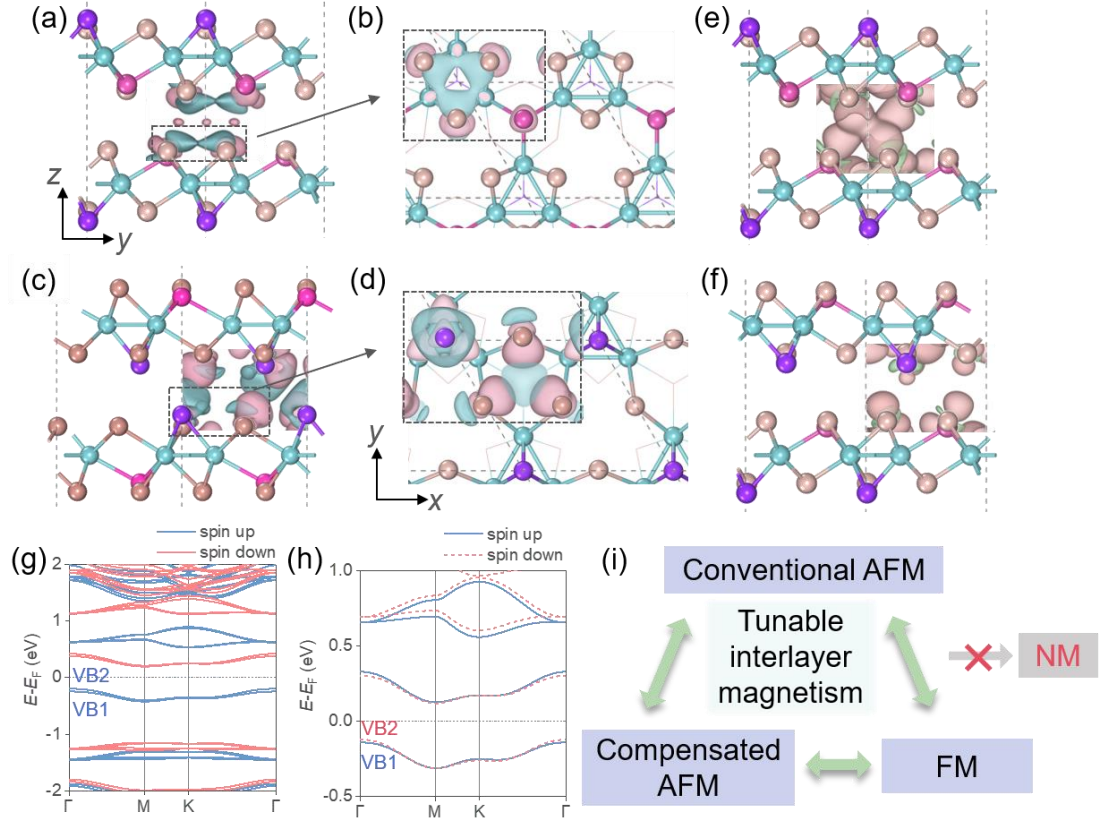


Fig. 4 (a) Side view of the L1 stacking of Nb_3Cl_8 . The isosurface represents the interfacial differential charge density (DCD), with red indicating charge accumulation and blue indicating charge reduction. (b) Top view of the DCD from the dashed box in (a). (c-d) Same as (a-b) but for the C2 stacking of Nb_3Cl_8 . (e-f) Side view of the L1 (e) and 4-R60-UU (f) stacking of Nb_3Cl_8 . The isosurface represents the spin density in the interlayer FM coupling configuration, with orange for spin-up and green for spin-down. (g) Band structure of Nb_3Cl_8 with 4-R60-UU stacking in the FM configuration. (h) Band structure of Nb_3Cl_8 with AA (1-R0-UU) stacking in the AFM configuration. (i) Illustration of tunable interlayer magnetism in the Nb_3X_8 system. Interlayer DCDs are shown with an isosurface value of $1 \times 10^{-4} \text{ e/Bohr}^3$. Spin densities are shown with an isosurface value of $5 \times 10^{-4} \text{ e/Bohr}^3$.

We further examine how interlayer coupling modulates the favored magnetic configuration in Nb_3X_8 bilayers. Total energy comparisons among different magnetic configurations [Fig. 2 (f-h) and Fig. S5] reveal that most (71 out of 96) stacking configurations strongly favor interlayer AFM, while 22 out of 96 exhibit nearly degenerate interlayer AFM and FM states, with the energy difference between them being less than 0.1 meV/Nb_3 . However, interlayer FM becomes more stable in the 4-R60-UU stacking in Nb_3X_8 ($\text{X} = \text{Cl}, \text{Br}, \text{I}$) [Fig. 4(f)]. To illustrate the mechanism of

interlayer magnetic coupling, we use the L1 and 4-R60-UU stackings of Nb₃Cl₈ as prototypical examples. In Nb₃Cl₈, the L1 stacking configuration exhibits the largest energy difference $E(\text{FM}) - E(\text{AFM}) = 23.4 \text{ meV/Nb}$. The spin density of the FM configuration in the L1 stacking [Fig. 4(e)] exhibits significant interlayer overlap, which enhances Pauli repulsion. This Pauli repulsion favors interlayer AFM coupling, which outweighs the FM tendency induced by interlayer hopping and thus stabilizes a relatively strong interlayer AFM ground state in the L1 stacking. [61]. In contrast, the interlayer overlapping is largely reduced in the 4-R60-UU configuration [Fig. 4(f)], leading to weaker Pauli repulsion. As a result, interlayer hopping dominates over Pauli repulsion the interlayer magnetic interaction, giving rise to interlayer FM coupling[61]. We plotted its FM band structure in Fig. 4(g). The splitting of the two VBs (noted VB1 and VB2) at the Γ point is 49 meV (42 meV for the two CBs, noted CB1 and CB2), while VB1 and VB2 are degenerate at the K point. The visualized wavefunction at the K point shows that the spin-up component of VB1 and the spin-down component of CB1 are identical, as well as for VB2 and CB1 [Fig. S9(b-e)], which is consistent with the characteristics of a Mott insulator and confirms that the system retains its Mott insulator character. In summary, the interlayer magnetic coupling is determined by the competition between interlayer Pauli repulsion (which favors antiferromagnetism, AFM) and interlayer hopping (which favors ferromagnetism, FM). Since the orbitals contributing to the magnetic moment in Nb₃X₈ are predominantly distributed within the Nb atomic layers, the interlayer coupling is relatively weak. As a result, the wavefunctions of opposite spins from the two layers cannot overlap interlayer to form covalent bonds, leading to a NM state with relatively high energy.

Those 71 energetically favored AFM configurations can be categorized into, at least, two types of different spin groups. In every configuration with a R60 twisting angle in anti-parallel polarization alignments (up to eight configurations for each halide), an inversion symmetry connects the two spin sublattices, resulting in conventional AFM states with spin-degenerate bands developing throughout the Brillouin zone (BZ) [see Fig. S4(c) for the L1 stacked Nb₃Cl₈ bilayer]. However, every UU-polarized or every R0 (untwisted) configuration (totally up to 16 for each halide)

exhibits an AFM configuration where no symmetry relates the two spin sublattices. The lack of symmetry yields a compensated AFM [61] state with appreciable spin splitting between the spin-up and -down bands throughout the entire Brillouin zone. The simplest structure of compensated AFM is the AA stacked configurations (1-R0-UU). Figure 4(l) shows the band structure of a compensated AFM AA stacking of Nb₃Cl₈, where the maximum splitting of up to 26 meV occurs among the four VBs and CBs near the Fermi level, particularly in the VB1 and VB2 at the Γ point. Therefore, Nb₃X₈ bilayers exhibit stacking tunable interlayer magnetism, ranging from FM, AFM-FM degeneracy, conventional AFM, to compensated AFM. Although purely electric-field-driven polarization switching in Nb₃Cl₈ remains challenging, combining electric fields with thermal activation, tensile strain, charge doping, or scanning-probe-tip manipulation offers feasible pathways for tuning interlayer magnetism.

Previous magnetic susceptibility measurements report that bulk Nb₃Cl₈ and Nb₃Br₈ behave as Curie-Weise paramagnets at high temperature but appear NM in their LT phases [32,34,35]. Two microscopic mechanisms were proposed to explain the origin of this NM behavior, namely inter-layer charge disproportionation[34] and formation of band insulator through interlayer interactions [35,63]. Although DFT is not designed to fully capture PM, it can directly describe non-magnetic states arising from either mechanism. Because both mechanisms require interlayer coupling, the smallest structural motif that can host them is a bilayer. Our exhaustive DFT calculations for all bilayers of four Nb₃X₈ compounds, however, reveal neither of these effects in any stacking considered. We further optimized the geometric structures of the LT phase of bulk Nb₃Cl₈ and Nb₃Br₈ using the NM configuration and compared their energies in NM, and interlayer AFM and FM configurations. In every case, the interlayer AFM state is energetically more favored than the NM and interlayer FM states. The energy difference between the NM and interlayer AFM states ($E_{\text{NM}} - E_{\text{AFM}}$) increases monotonically with the on-site Hubbard U , consistent with our results for bilayer calculations. These results indicate that, within the DFT(+U) framework, the ground state of LT-phase bulk Nb₃Cl₈ and Nb₃Br₈ is most plausibly an interlayer AFM Mott insulator. This assignment is not inconsistent with the nearly featureless LT

susceptibility reported experimentally. Should the true ground state prove to be strictly non-magnetic, its origin must involve physics beyond standard DFT (+U), which calls for further investigations.

In summary, we found that in Nb_3X_8 bilayers, all magnetic ground states are interlayer AFM, with a few degenerate FM states, exhibiting tunable interlayer AFM. However, whether in bilayers or bulk, the NM states have much higher energies than the magnetic ground states, suggesting that previous understanding may need revision or that beyond-DFT-level theoretical calculations are required for a better understanding. Through the analysis of the electronic structure and the linear dependence of band splitting with U , we found that all considered bilayers are Mott insulators, indicating robust Mott insulating behavior in this system. Regardless of the interlayer magnetic coupling, the Mott insulating nature persists, which contrasts with the previous assumption that the system could exhibit a NM state. The robustness of the Mott insulator state and the absence of an NM phase in Nb_3X_8 contrast with NbSe_2 . In NbSe_2 , the interfacial Se atoms have out-of-plane p_z orbitals, which results in strong interlayer coupling, allowing unpaired electrons to form interlayer bonds[63]. In contrast, in Nb_3X_8 , the states near the Fermi level are primarily derived from Nb orbitals, with a much smaller contribution from halogen atoms. As a result, the interlayer coupling in Nb_3X_8 is much weaker. Our study provides unexpected results and insights into the role of interlayer coupling in modulating correlated insulators, contributing to the further development of this field.

References

- [1] Han X, Chen H, Tan H, Cao Z, Huang Z, Ye Y, Zhao Z, Shen C, Yang H, Yan B, Wang Z and Gao H-J 2025 Atomic manipulation of the emergent quasi-2D superconductivity and pair density wave in a kagome metal *Nat. Nanotechnol.*
- [2] Yin J-X, Lian B and Hasan M Z 2022 Topological kagome magnets and superconductors *Nature* **612** 647–57
- [3] Wang Y, Wu H, McCandless G T, Chan J Y and Ali M N 2023 Quantum states and intertwining phases in kagome materials *Nat Rev Phys* **5** 635–58
- [4] Zhang Z, Dai J, Wang C, Zhu H, Pang F, Cheng Z and Ji W 2025 2D Kagome Materials: Theoretical Insights, Experimental Realizations, and Electronic Structures *Adv Funct Materials* **35** 2416508
- [5] Yan S, Huse D A and White S R 2011 Spin-Liquid Ground State of the $S = 1/2$ Kagome Heisenberg Antiferromagnet **332**
- [6] Huang Z, Chen H, Zhang Z, Zhang H, Zhao Z, Wang R, Yang H, Ji W, Wang Z and Gao H-J 2025 Spatially anisotropic Kondo resonance intertwined with superconducting gap in kagome metal $\text{CsV}_3\text{-xCrSb}_5$
- [7] Chen H, Yang H, Hu B, Zhao Z, Yuan J, Xing Y, Qian G, Huang Z, Li G, Ye Y, Ma S, Ni S, Zhang H, Yin Q, Gong C, Tu Z, Lei H, Tan H, Zhou S, Shen C, Dong X, Yan B, Wang Z and Gao H-J 2021 Roton pair density wave in a strong-coupling kagome superconductor *Nature* **599** 222–8
- [8] Liu C-H, Wei A, Cheung M F and Perepichka D F 2022 Vanishing Electronic Band Gap in Two-Dimensional Hydrogen-Bonded Organic Frameworks *Chem. Mater.* **34** 3461–7
- [9] Dai J, Zhang Z, Pan Z, Wang C, Zhang C, Cheng Z and Ji W 2024 Kagome bands and magnetism in MoTe_{2-x} kagome monolayers
- [10] Ko W-H, Lee P A and Wen X-G 2009 Doped kagome system as exotic superconductor *Phys. Rev. B* **79** 214502
- [11] Lin T-Y, Song F-F and Zhang G-M 2025 Theory of charge-6e condensed phase in Kagome lattice superconductors *Phys. Rev. B* **111** 054508
- [12] Jiang H-M, Mao M, Miao Z-Y, Yu S-L and Li J-X 2024 Interplay between chiral charge density wave and superconductivity in kagome superconductors studied by self-consistent mean-field theory *Phys. Rev. B* **109** 104512
- [13] Neupert T, Denner M M, Yin J-X, Thomale R and Hasan M Z 2022 Charge order and superconductivity in kagome materials *Nat. Phys.* **18** 137–43
- [14] Ortiz B R, Teicher S M L, Hu Y, Zuo J L, Sarte P M, Schueller E C, Abeykoon A M M,

- Krogstad M J, Rosenkranz S, Osborn R, Seshadri R, Balents L, He J and Wilson S D 2020 Cs V₃ Sb₅: A Z₂ Topological Kagome Metal with a Superconducting Ground State *Phys. Rev. Lett.* **125** 247002
- [15] Xing Y, Shen J, Chen H, Huang L, Gao Y, Zheng Q, Zhang Y-Y, Li G, Hu B, Qian G, Cao L, Zhang X, Fan P, Ma R, Wang Q, Yin Q, Lei H, Ji W, Du S, Yang H, Wang W, Shen C, Lin X, Liu E, Shen B, Wang Z and Gao H-J 2020 Localized spin-orbit polaron in magnetic Weyl semimetal Co₃Sn₂S₂ *Nat Commun* **11** 5613
- [16] Morali N, Batabyal R, Nag P K, Liu E, Xu Q, Sun Y, Yan B, Felser C, Avraham N and Beidenkopf H 2019 Fermi-arc diversity on surface terminations of the magnetic Weyl semimetal Co₃Sn₂S₂ *Science* **365** 1286–91
- [17] Liu D F, Liang A J, Liu E K, Xu Q N, Li Y W, Chen C, Pei D, Shi W J, Mo S K, Dudin P, Kim T, Cacho C, Li G, Sun Y, Yang L X, Liu Z K, Parkin S S P, Felser C and Chen Y L 2019 Magnetic Weyl semimetal phase in a Kagomé crystal *Science* **365** 1282–5
- [18] Jovanovic M and Schoop L M 2022 Simple Chemical Rules for Predicting Band Structures of Kagome Materials *J. Am. Chem. Soc.* **144** 10978–91
- [19] Piquero-Zulaica I, Hu W, Seitsonen A P, Haag F, Küchle J, Allegretti F, Lyu Y, Chen L, Wu K, El-Fattah Z M A, Aktürk E, Klyatskaya S, Ruben M, Muntwiler M, Barth J V and Zhang Y 2024 Unconventional Band Structure via Combined Molecular Orbital and Lattice Symmetries in a Surface-Confined Metallated Graphdiyne Sheet *Advanced Materials* 2405178
- [20] Shi Z and Lin N 2009 Porphyrin-Based Two-Dimensional Coordination Kagome Lattice Self-Assembled on a Au(111) Surface *J. Am. Chem. Soc.* **131** 5376–7
- [21] Mo Y-P, Liu X-H and Wang D 2017 Concentration-Directed Polymorphic Surface Covalent Organic Frameworks: Rhombus, Parallelogram, and Kagome *ACS Nano* **11** 11694–700
- [22] Furukawa S, Uji-i H, Tahara K, Ichikawa T, Sonoda M, De Schryver F C, Tobe Y and De Feyter S 2006 Molecular Geometry Directed Kagomé and Honeycomb Networks: Toward Two-Dimensional Crystal Engineering *J. Am. Chem. Soc.* **128** 3502–3
- [23] Dai J, Zhang Z, Pan Z, Wang C, Zhang C, Cheng Z and Ji W 2024 Kagome bands and magnetism in MoTe_{2-x} kagome monolayers
- [24] Pan Z, Xiong W, Dai J, Zhang H, Wang Y, Jian T, Cui X, Deng J, Lin X, Cheng Z, Bai Y, Zhu C, Huo D, Li G, Feng M, He J, Ji W, Yuan S, Wu F, Zhang C and Gao H-J 2025 Ferromagnetism and correlated insulating states in monolayer Mo₃₃Te₅₆ *Nat Commun* **16** 3084
- [25] Lei L, Dai J, Dong H, Geng Y, Cao F, Wang C, Xu R, Pang F, Liu Z-X, Li F, Cheng Z, Wang G and Ji W 2023 Electronic Janus lattice and kagome-like bands in coloring-triangular

- [26] Wu Q, Quan W, Pan S, Hu J, Zhang Z, Wang J, Zheng F and Zhang Y 2024 Atomically Thin Kagome-Structured Co₉Te₁₆ Achieved through Self-Intercalation and Its Flat Band Visualization *Nano Lett.* [acs.nanolett.4c01526](https://doi.org/10.1021/acs.nanolett.4c01526)
- [27] Zhang Z-M, Gong B-C, Nie J-H, Meng F, Zhang Q, Gu L, Liu K, Lu Z-Y, Fu Y-S and Zhang W 2023 Self-Intercalated 1T-FeSe₂ as an Effective Kagome Lattice *Nano Lett.* **23** 954–61
- [28] Wang 王 R 人宏, Wang 王 C 聪, Li 李 R 睿宣, Guo 郭 D 的坪, Dai 戴 J 佳琦, Zong 宗 C 灿波, Zhang 张 W 伟涵 and Ji 季 W 威 2025 High-throughput discovery of kagome materials in transition metal oxide monolayers *Chinese Phys. B* **34** 046801
- [29] Zhang Y, Gu Y, Weng H, Jiang K and Hu J 2023 Mottness in two-dimensional van der Waals Nb₃X₈ monolayers (X = Cl, Br, and I) *Phys. Rev. B* **107** 035126
- [30] Date M, Petocchi F, Yen Y, Krieger J A, Pal B, Hasse V, McFarlane E C, Körner C, Yoon J, Watson M D, Strocov V N, Xu Y, Kostanovski I, Ali M N, Ju S, Plumb N C, Sentef M A, Woltersdorf G, Schüler M, Werner P, Felser C, Parkin S S P and Schröter N B M 2025 Momentum-resolved fingerprint of Mottness in layer-dimerized Nb₃Br₈ *Nat Commun* **16** 4037
- [31] Hu J, Zhang X, Hu C, Sun J, Wang X, Lin H-Q and Li G 2023 Correlated flat bands and quantum spin liquid state in a cluster Mott insulator *Commun Phys* **6** 1–8
- [32] Gao S, Zhang S, Wang C, Yan S, Han X, Ji X, Tao W, Liu J, Wang T, Yuan S, Qu G, Chen Z, Zhang Y, Huang J, Pan M, Peng S, Hu Y, Li H, Huang Y, Zhou H, Meng S, Yang L, Wang Z, Yao Y, Chen Z, Shi M, Ding H, Yang H, Jiang K, Li Y, Lei H, Shi Y, Weng H and Qian T 2023 Discovery of a Single-Band Mott Insulator in a van der Waals Flat-Band Compound *Phys. Rev. X* **13** 041049
- [33] Grytsiuk S, Katsnelson M I, Loon E G C P van and Rösner M 2024 Nb₃Cl₈: a prototypical layered Mott-Hubbard insulator *npj Quantum Mater.* **9** 1–13
- [34] Haraguchi Y, Michioka C, Ishikawa M, Nakano Y, Yamochi H, Ueda H and Yoshimura K 2017 Magnetic–Nonmagnetic Phase Transition with Interlayer Charge Disproportionation of Nb₃ Trimers in the Cluster Compound Nb₃Cl₈ *Inorg. Chem.* **56** 3483–8
- [35] Sheckelton J P, Plumb K W, Trump B A, Broholm C L and McQueen T M 2017 Rearrangement of van der Waals stacking and formation of a singlet state at T = 90 K in a cluster magnet *Inorg. Chem. Front.* **4** 481–90
- [36] Sun Z, Zhou H, Wang C, Kumar S, Geng D, Yue S, Han X, Haraguchi Y, Shimada K, Cheng P, Chen L, Shi Y, Wu K, Meng S and Feng B 2022 Observation of Topological Flat

Bands in the Kagome Semiconductor Nb₃Cl₈ *Nano Lett.* **22** 4596–602

- [37] Zhao Y, Qiao J, Yu P, Hu Z, Lin Z, Lau S P, Liu Z, Ji W and Chai Y 2016 Extraordinarily Strong Interlayer Interaction in 2D Layered PtS₂ *Advanced Materials* **28** 2399–407
- [38] Qiao J, Kong X, Hu Z-X, Yang F and Ji W 2014 High-mobility transport anisotropy and linear dichroism in few-layer black phosphorus *Nat Commun* **5** 4475
- [39] Splendiani A, Sun L, Zhang Y, Li T, Kim J, Chim C-Y, Galli G and Wang F 2010 Emerging Photoluminescence in Monolayer MoS₂ *Nano Lett.* **10** 1271–5
- [40] Wang C, Zhou X, Zhou L, Tong N-H, Lu Z-Y and Ji W 2019 A family of high-temperature ferromagnetic monolayers with locked spin-dichroism-mobility anisotropy: MnNX and CrCX (X = Cl, Br, I; C = S, Se, Te) *Science Bulletin* **64** 293–300
- [41] Hu Z-X, Kong X, Qiao J, Normand B and Ji W 2016 Interlayer electronic hybridization leads to exceptional thickness-dependent vibrational properties in few-layer black phosphorus *Nanoscale* **8** 2740–50
- [42] Zhang Z, Wang C, Guo P-J, Zhou L, Pan Y, Hu Z and Ji W 2025 Interlayer coupling driven rotation of the magnetic easy axis in MnS_e 2 monolayers and bilayers *Phys. Rev. B* **111** 054422
- [43] Wang C, Zhou X, Pan Y, Qiao J, Kong X, Kaun C-C and Ji W 2018 Layer and doping tunable ferromagnetic order in two-dimensional Cr S₂ layers *Phys. Rev. B* **97** 245409
- [44] Jiang P, Wang C, Chen D, Zhong Z, Yuan Z, Lu Z-Y and Ji W 2019 Stacking tunable interlayer magnetism in bilayer CrI_3 *Phys. Rev. B* **99** 144401
- [45] Huang B, Clark G, Navarro-Moratalla E, Klein D R, Cheng R, Seyler K L, Zhong D, Schmidgall E, McGuire M A, Cobden D H, Yao W, Xiao D, Jarillo-Herrero P and Xu X 2017 Layer-dependent ferromagnetism in a van der Waals crystal down to the monolayer limit *Nature* **546** 270–3
- [46] Rogée L, Wang L, Zhang Y, Cai S, Wang P, Chhowalla M, Ji W and Lau S P 2022 Ferroelectricity in untwisted heterobilayers of transition metal dichalcogenides *Science* **376** 973–8
- [47] Li L and Wu M 2017 Binary Compound Bilayer and Multilayer with Vertical Polarizations: Two-Dimensional Ferroelectrics, Multiferroics, and Nanogenerators *ACS Nano* **11** 6382–8
- [48] Perdew J P, Burke K and Ernzerhof M 1996 Generalized Gradient Approximation Made Simple *Phys. Rev. Lett.* **77** 3865–8
- [49] Blöchl P E 1994 Projector augmented-wave method *Phys. Rev. B* **50** 17953–79
- [50] Kresse G and Furthmüller J 1996 Efficient iterative schemes for ab initio total-energy

calculations using a plane-wave basis set *Phys. Rev. B* **54** 11169–86

- [51] Grimme S, Antony J, Ehrlich S and Krieg H 2010 A consistent and accurate ab initio parametrization of density functional dispersion correction (DFT-D) for the 94 elements H–Pu *The Journal of Chemical Physics* **132** 154104
- [52] Dudarev S L, Botton G A, Savrasov S Y, Humphreys C J and Sutton A P 1998 Electron-energy-loss spectra and the structural stability of nickel oxide: An LSDA+U study *Phys. Rev. B* **57** 1505–9
- [53] Conte F, Ninno D and Cantele G 2020 Layer-dependent electronic and magnetic properties of Nb₃I₈ *Phys. Rev. Research* **2** 033001
- [54] Feng Y 2023 Enabling triferroics coupling in breathing kagome lattice Nb₃X₈ (X = Cl, Br, I) monolayers *Journal of Materials Chemistry C*
- [55] Aretz J, Grytsiuk S, Liu X, Feraco G, Knekna C, Waseem M, Dan Z, Bianchi M, Hofmann P, Ali M N, Katsnelson M I, Grubišić-Čabo A, Strand H U R, Loon E G C P van and Rösner M 2025 From strong to weak correlations in breathing-mode kagome van der Waals materials: Nb₃(F,Cl,Br,I) as a robust and versatile platform for many-body engineering
- [56] Regmi S, Sakhya A P, Fernando T, Zhao Y, Jeff D, Sprague M, Gonzalez F, Bin Elius I, Mondal M I, Valadez N, Jarrett D, Agosto A, Yang J, Chu J-H, Khondaker S I, Xu X, Cao T and Neupane M 2023 Observation of flat and weakly dispersing bands in the van der Waals semiconductor Nb₃Br₈ with breathing kagome lattice *Phys. Rev. B* **108** L121404
- [57] Magonov S N, Zoennchen P, Rotter H, Cantow H J, Thiele G, Ren J and Whangbo M H 1993 Scanning tunneling and atomic force microscopy study of layered transition metal halides Nb₃X₈ (X = Cl, Br, I) *J. Am. Chem. Soc.* **115** 2495–503
- [58] Kim B J, Jeong B J, Oh S, Chae S, Choi K H, Nanda S S, Nasir T, Lee S H, Kim K-W, Lim H K, Chi L, Choi I J, Hong M-K, Yi D K, Yu H K, Lee J-H and Choi J-Y 2019 Structural and Electrical Properties of Nb₃I₈ Layered Crystal *Phys. Status Solidi RRL*
- [59] Pasco C M, El Baggari I, Bianco E, Kourkoutis L F and McQueen T M 2019 Tunable Magnetic Transition to a Singlet Ground State in a 2D van der Waals Layered Trimerized Kagomé Magnet *ACS Nano* **13** 9457–63
- [60] Liu H 2025 Direct Evidence of Intrinsic Mott State and Its Layer-Parity Oscillation in a Breathing Kagome Crystal Down to Monolayer *PHYSICAL REVIEW LETTERS*
- [61] Wang C, Zhou X, Zhou L, Pan Y, Lu Z-Y, Wan X, Wang X and Ji W 2020 Bethe-Slater-curve-like behavior and interlayer spin-exchange coupling mechanisms in two-dimensional magnetic bilayers *Phys. Rev. B* **102**
- [62] Mazin I and The PRX Editors 2022 Editorial: Altermagnetism---A New Punch Line of

- [63] Dai J, Qiao J, Wang C, Zhou L, Wu X, Liu L, Song X, Pang F, Cheng Z, Kong X, Wang Y and Ji W 2023 Layer Sliding And Twisting Induced Electronic Transitions In Correlated Magnetic 1t-Nbse₂ Bilayers *Adv. Funct. Mater.*